Waste Management 176 (2024) 52–63

Contents lists available at ScienceDirect

Waste Management

journal homepage: www.elsevier.com/locate/wasman

Research Paper

The effect of nano-silica and silica fume on the sodium carbonate-activated slag system containing air pollution control residues

Xuan Ling [a,b], Katrin Schollbach [b], Yuxuan Chen [b,c,*], H.J.H. Brouwers [a,b]

[a] State Key Laboratory of Silicate Materials for Architectures, Wuhan University of Technology, Wuhan 430070, China
[b] Department of the Built Environment, Eindhoven University of Technology, 5612 AP Eindhoven, the Netherlands
[c] School of Civil Engineering, Wuhan University, Wuhan 430072, China

ARTICLE INFO

Keywords:
Olivine nano-silica
Silica fume
Carbonation
Blast furnace slag
Incineration filter dust

ABSTRACT

The utilization of municipal solid waste incineration residues in alkali-activated granulated ground blast furnace slag (GGBFS) has garnered substantial interest for its potential in sustainable solid waste management and achieving a low-carbon footprint. However, incorporating these residues often leads to the deterioration of mechanical properties. This study revealed the role of silica fume (SF) and nano-silica (NS) derived from olivine within a sodium carbonate-activated GGBFS system incorporating air pollution control (APC) residues. The dosage of silica additives and APC residues ranges from 0 – 6 wt% and 0–15 wt%, respectively. The mechanical properties, reaction kinetics, phase composition, microstructure and carbonation resistance of the blended binder were investigated. Results indicated that SF slightly improved the early compressive strength with the formation of C-(A)-S-H gel (Ca/Si = 1.47, Al/Si = 0.23), hemicarboaluminate and hydrotalcite; reactive NS retarded the activation of GGBFS and inhibited the formation of hemicarboaluminate and hydrotalcite, while promoting the formation of C-A-S-H gel (Ca/Si = 1.01, Al/Si = 0.23), resulting in an impressive 80.3 % enhancement in compressive strength. Notably, NS-modified samples exhibited decreased carbonation resistance due to increased porosity and C-(A)-S-H gels that are vulnerable to carbonation. Conversely, 2 % SF addition decreased the diffusion rate of CO_2, and APC residues improved the carbonation resistance by facilitating the formation of C-(A)-S-H gel with a higher Ca/Si ratio. This study provided an alternative management practice for APC residues with favorable early strength development and offered new insights into using silica additives to enhance waste-combined alkali-activated materials.

1. Introduction

In recent years, alkali-activated materials (AAMs), proposed as sustainable binders for their low CO_2 emissions during manufacturing, have been widely tested (Shi et al., 2011; Shi and Qian, 2000; Wang et al., 1995). These binders are produced by mixing solid precursors with an alkaline activator solution, exhibiting high mechanical performance, excellent durability, low thermal conductivity and high resistance to chemical attack (Lu and Poon, 2018; Shi et al., 2018b; Wang et al., 2016). However, the employed activators, such as hydroxides and silicates, are highly alkaline, posing safety risks during formulation, and their production is energy intensive (Li et al., 2019; Shi et al., 2018a). To address these concerns, activators with lower alkalinity, such as sodium carbonate and sodium sulphate, have been employed in AAMs (Adesina, 2021; Walling et al., 2018). Yuan et al. reported excellent mechanical performance of sodium carbonate-activated slag at later ages (Yuan et al., 2017b). Nevertheless, the sodium carbonate-activated slag system often exhibits prolonged setting time and delayed compressive strength development. These characteristics are associated with the slower dissolution of silicate species due to the relatively lower initial pH of the sodium carbonate activator. On the other hand, Ca^{2+} ions released from the slag first react with CO_3^{2-} from the activator, forming carbonate salts like calcite and gaylussite (Bernal et al., 2014). The C-(A)-S-H gel, the major binding reaction product in AAMs, precipitates after the depletion of CO_3^{2-} ions, consequently resulting in an extended hardening process.

For the purpose of accelerating the reaction process, several types of additives have been proposed for use in the sodium carbonate-activated slag, such as the calcined layered double hydroxides (CLDH), calcined dolomite, calcium carbide residue and $Ca(OH)_2$ (Gao et al., 2021; Jeon et al., 2015; Ke et al., 2016; Yang et al., 2012, 2019). These additives

* Corresponding author.
E-mail address: yuxuan.chen@whu.edu.cn (Y. Chen).

https://doi.org/10.1016/j.wasman.2024.01.028
Received 3 January 2023; Received in revised form 25 August 2023; Accepted 14 January 2024

facilitate the removal of CO_3^{2-} ions by the formation of carbonates and generate OH^- ions within the aqueous phase to enhance the alkalinity. Meanwhile, the Ca^{2+} ions released from these additives contribute to the polymerization of C-(A)-S-H gel. A similar acceleration result was achieved in our previous study, wherein waste incineration filter dust (WIFD), an air pollution control residue from municipal solid waste incineration (MSWI) containing considerable amounts of portlandite and calcite, was incorporated into the sodium carbonate-activated slag system (Ling et al., 2021). Unfortunately, the utilization of WIFD results in a reduction of the mechanical performance of sodium carbonate-activated slag. Similar degradation in mechanical properties is documented while recycling other types of solid waste residues in AAMs (Liu et al., 2021, 2016; Shirley and Black, 2011; Zhao et al., 2021), as presented in **Supplementary Table S1**. For instance, the inclusion of 40 % non-reactive bottom ash leads to a 50 % reduction in the compressive strength of alkali-activated slag at 28 d (Gao et al., 2017b). Compared with the traditional aluminosilicate precursors, solid waste materials have relatively lower pozzolanic reactivity. Consequently, the reduced gel formation influences the mechanical properties of the resulting cementitious materials. Thus, a thorough understanding of the enhancement of mechanical properties in solid waste-combined binders is of vital importance for their application in construction materials, which also contributes to a more sustainable industry and improved solid waste management. The performance of AAMs depends on the properties of the precursors and alkaline activators, curing conditions, and water/binder (w/b) ratio (Ben Haha et al., 2011; Gebregziabiher et al., 2016; Provis and van Deventer, 2019; Yuan et al., 2018; Živica, 2007). The influence of these parameters on reaction kinetics, mechanical properties and durability have been intensively investigated (Bernal et al., 2012a; Gao et al., 2015a). However, the incorporation of solid waste materials will inherently affect the reaction system of AAMs, consequently impacting their overall performance. Hence, a more comprehensive analysis of the reaction mechanisms and processes becomes crucial, considering the chemical and phase composition variations of the added solid waste materials from diverse sources.

It has been acknowledged nanomaterial, including $CaCO_3$ (Meng et al., 2017), Al_2O_3 (Liu et al., 2019), and TiO_2 (Wang et al., 2020b), SiO_2 (Gao et al., 2015b; Nikravan et al., 2018), can enhance the mechanical properties of binders. The enhancement is attributed to their nano-filling effect, which optimizes particle arrangement and reduces voids. Additionally, nanomaterials serve as nucleation sites, promoting the formation of gel products in alkali-activated materials. Notably, nano-silica (NS) and silica fume (SF) are favoured due to their pozzolanic reactivity and ability to form more C-(A)-S-H gels (Quercia et al., 2012). NS induces the formation of C-(A)-S-H gel with higher density through accelerated polymerization of silicate chains (Singh et al., 2017), thereby expectedly refining pore structures and improving the mechanical properties of the modified binders (Gao et al., 2015b). Comparative studies on the effect of SF and NS on the performance of both Ordinary Portland cement (OPC) and AAMs have been conducted (Nikravan et al., 2018; Ramezanianpour and Moeini, 2018). However, it is important to note that the alkali-activated reaction system differs from that of OPC, particularly in terms of alkali involvement. While portlandite forms during cement hydration, alkali activators are consumed to dissolve aluminosilicate precursors in AAMs. The competition between silica additives and aluminosilicate precursors for OH^- ions emerges as a significant factor influencing the performance of AAMs. Despite extensive investigation into the influence of SF and NS on AAMs (Ramezanianpour and Moeini, 2018), most research has primarily focused on sodium hydroxide, potassium hydroxide, and sodium silicate-activated AAMs. There is a scarcity of reports on the performance of sodium carbonate-activated slag modified with silica additives, particularly in the context of WIFD, thus hindering the broader application of cost-effective and environmentally friendly sodium carbonate-activated materials.

Notably, aside from silica additives, the incorporation of portlandite from the utilized WIFD significantly impacts the formation of C-(A)-S-H gel. This influence arises due to their structural characteristic, particularly concerning the interlayer distance, which is correlated with the initial Ca/Si ratio of the raw precursors. (Kapeluszna et al., 2017). Specifically, the basal spacing decreases from 14.17 \AA to 11.74 \AA when the Ca/Si ratio in C-(A)-S-H gel increases from 0.8 to 1.1 and remains quite constant when the Ca/Si is beyond 1.1 (Renaudin et al., 2009). However, there is limited available information regarding the relationship between the Ca/Si ratio, silica additives and the gel composition in the sodium carbonate-activated slag systems. Hence, the role of the initial Ca/Si ratio on the blended binder was addressed as well for the effective utilization of WIFD.

Furthermore, the carbonation resistance of AAMs is considered an important aspect of their durability. The diffusion of CO_2 in AAMs reduces the pH in the pore solution (Pacheco Torgal et al., 2012). Since sufficient protection of steel rebar requires a pH between 12 and 14, the carbonation resistance dictates the corrosion resistance and service duration of the reinforcing steel (Pacheco Torgal et al., 2012). Previous research on the carbonation of AAMs focused on alkali-silicate or hydroxide as the activator (Bernal et al., 2012b; S. Y. Wang et al., 2020a). In contrast, few studies have reported the carbonation resistance of the reaction systems using sodium carbonate as the activator. Given that the early strength development of sodium carbonate-activated slag materials can be accelerated by WIFD, the present work comprehensively characterizes and offers new insights into the carbonation behaviour with varying silica additives and WIFD dosages.

Therefore, SF and NS were utilized to improve the performance of alkali-activated slag with WIFD. The primary objective of this study is to investigate the effect of silica additives and the initial Ca/Si ratio of the binder on the valorization of WIFD in the sodium carbonate-activated slag. The mechanical properties, reaction kinetics, microstructure, and composition of the reaction products are intensively studied with multiple characterization techniques. Moreover, the present work advances the current understanding of the degradation mechanisms of sodium carbonate-activated slag binders prepared with various silica additives exposed to a CO_2 environment.

2. Experimental program

2.1. Materials

The ground granulated blast furnace slag (GGBFS) sourced from ENCI (Ijmuiden, Netherlands) and waste incineration filter dust (WIFD) obtained from Euro Trust Management (Netherlands) were used as the primary materials for producing the sodium carbonate-activated slag in this study. The raw WIFD was derived from a Dutch MSWI plant, generated through the injection of a suspension of quick lime into the hot flue gas. It primarily consists of calcite and portlandite (see Supplementary **Figure S1**), along with certain chloride and sulphate salts, as confirmed by the results of one-batch leaching test provided in **Supplementary Table S2**. No additional treatment was conducted before its combination with GGBFS. Sodium carbonate (powder, analytical grade) was supplied by Sigma-Aldrich. Silica fume (SF) (Elkem 920ED) and nano-silica (NS) were used as the silica source in this study. Nano-silica (Euro support, Netherlands) was produced by dissolving olivine in 3 M sulfuric acid (Lázaro García, 2014). The procedure is provided in **Supplementary Text S1**. Detailed information on raw materials is provided in **Supplementary Text S2**.

2.2. Mixture design and preparations

The group Ref consisted of 10 wt% WIFD and 90 wt% GGBFS mixed with sodium carbonate with an equivalent Na_2O concentration of 3.5 %. Considering that optimal mechanical strength can be achieved by 4 wt% SF in sodium carbonate-activated materials according to (Cheah et al., 2019), the effect of SF and NS on the performance of the blended binder

was investigated by adding 2 %, 4 % and 6 % by mass of the total binder, respectively. In addition, the influence of the initial Ca/Si ratio in the raw material was investigated with a constant silica content of 4 wt%, as shown in Table 1. The Ca/Si ratio was varied as 0.93, 0.99, and 1.05 to clarify the effect of basal spacing changes of the C-(A)-S-H gels on the performance of the binder, whereas the Al/Si ratio was controlled by adjusting the proportion of WIFD and GGBFS in the reaction system. The procedure of specimen preparation is provided in **Supplementary Text S3**. Samples were cast into 40 × 40 × 160 mm^3 moulds, covered with plastic films for 24 h before demolding and sealed with plastic films. Curing was conducted under a laboratory condition at 20 ± 0.5 °C and 50 ± 5 % relative humidity.

2.3. Methodology

2.3.1. Flowability, pH value and mechanical performance of mortar

The flowability of the fresh mortar was determined using the mini spread flow table test in accordance with EN 1015–3:2007. A standard conical ring (Hägermann cone 70 mm diam. × 100 mm diam. × 60 mm ht) was filled with fresh mortar. Two perpendicular diameters were measured after 15 impacts and their average value was considered the slump flow of each mixture.

For the initial pH value test, two paste samples were prepared for each recipe. After mixing and stirring, the pH detector (Voltcraft pH-100ATC) was immediately inserted into the fresh paste. Record the value when the readings stabilize and calculate the average as the pH value.

After 7 d, 28 d and 180 d, the compressive strength of the mixture was tested according to EN 196–1:2005. Six samples were tested with a loading rate of 2400 N/s for each mortar and the average value was considered the compressive strength of each mixture.

2.3.2. Isothermal calorimeter

The reaction kinetics of all mixtures were analyzed by an isothermal calorimeter (TAM Air, Thermometric) at 25 °C. Paste samples listed in Table 1 were prepared and injected into a sealed glass ampoule for 7 d calorimetric tests. Heat flow and total heat release were normalized by the total mass of the solid. The initial peak occurring within the first few minutes due to the dissolution of raw precursors was excluded from the analysis. The results of all mixtures were recorded starting 30 min after sample mixing.

2.3.3. Phase assemblage analysis

The phase composition of paste samples was identified by X-ray diffraction (XRD), thermo-gravimetric (TG) and Fourier transform infrared spectroscopy (FT-IR). The procedures for sample preparation and test parameters are provided in **Supplementary Text S4**.

2.3.4. Microstructure analysis

The analysis was carried out employing a scanning electron microscope (SEM) with an energy-dispersive X-ray diffraction (EDX) (15KV) detector (Phenom Pro). The morphology images were collected with the backscattered electron (BSE). The microstructure of NS and SF were observed by JEOL JEM-1400 Plus transmission electron microscopy. The images were captured by a charge-coupled device (CCD) camera. The procedure for sample preparation is provided in **Supplementary Text S5**.

The nitrogen sorption analysis was conducted using a TriStar II 3020 instrument (Micrometrics). The powder samples were dried in a vacuum oven at 60 °C before the test. The gel pore size distribution was calculated by the Barrett-Joyner-Hallenda (BJH) method from the adsorption branch (Brunauer et al., 1938). Brunauer–Emmett–Teller (BET) surface area of each sample was characterized.

2.3.5. Carbonation resistance

After 28 d of curing, the samples were moved into a carbonation chamber. The relative humidity was set to 65 % according to the reported optimal value for carbonation (Leemann and Moro, 2017). The temperature was set at 25 °C, and a circular airflow with 3 % CO_2 gas by volume was applied in the chamber continuously during the test. These parameters are widely used in carbonation resistance evaluation (Bernal et al., 2013).

Table 1
Mix proportions of paste and mortar specimens.

	WIFD %	GGBFS %	SF %	NS %	w/b	Ca/Si	Al/Si
Ref	10	90	0	0	Paste = 0.5	1.12	0.36
S2R1.05	9.8	88.2	2	0		1.05	0.34
S4R1.05	14.0	82.0	4	0	Mortar	1.05	0.32
S4R0.99	9.6	86.4	4	0	=0.6	0.99	0.32
S4R0.93	5.2	90.8	4	0		0.93	0.32
S6R0.93	9.4	84.6	6	0		0.93	0.30
N2R1.05	9.8	88.2	0	2		1.05	0.34
N4R1.05	14.0	82.0	0	4		1.05	0.32
N4R0.99	9.6	86.4	0	4		0.99	0.32
N4R0.93	5.2	90.8	0	4		0.93	0.32
N6R0.93	9.4	84.6	0	6		0.93	0.30

Note: Superplasticizer 4 wt%, Na_2CO_3 6 wt% (3.5 wt% Na_2O).

3. Results

3.1. Flowability and compressive strength development

Fig. 1 **(a)** shows the flowability of the fresh mortar with different silica sources. The silica additives reduce the workability of all samples due to their smaller particle size. Notably, NS, with a higher specific surface area than silica fume, leads to a more pronounced reduction in the spreading flow. The flowability of the fresh mortar with different WIFD content is shown in Fig. 1 **(b)**, where SF or NS substitutes 4 wt% of the total binder. It is important to highlight that the flowability of the SF and NS modified mortar also decreases with increasing WIFD content owing to the higher water demand of WIFD [21]. The dissolution of portlandite in WIFD consumes free water. Moreover, the higher surface area of WIFD results in higher water adsorption, thereby and reduces the workability of the blends.

Fig. 1 **(c)** presents the compressive strength of the specimens with varying silica content. All the silica-modified samples demonstrate similar or higher compressive strength compared to the reference mortar at 7 d and 28 d. Specifically, the SF-modified samples exhibit a slight increase in compressive strength, whereas NS significantly promotes compressive strength at different ages, despite the reduction in spread flow. For instance, the sample with 4 % NS (N4R0.99) improves the compressive strength by 80.3 % compared to the reference at 28 d. A similar trend was also observed elsewhere (Li et al., 2004; Qing et al., 2007), suggesting a better enhancement of compressive strength by NS compared to SF. Furthermore, although Cheah et al. (Cheah et al., 2019) reported that the mortar with 4 % of SF exhibited the highest mechanical strength at 90 d, this study observed that the optimal 7 d and 28 d compressive strength was achieved with 6 % SF (S6R0.93). However, the S6R0.93 sample exhibit lower 180 d compressive strength than other SF-modified samples, indicating a lower contribution of SF as fillers at a later stage. Conversely, mortars prepared with NS can compensate for lower workability through improved paste-aggregate interfacial transition zone densification, leading to improved mechanical properties at 180 d due to the promoted formation of C-(A)-S-H gels (detailed discussion is provided in Section 3.3).

Fig. 1 **(d)** presents the compressive strength of the specimens with 4 % SF or NS. These specimens have different initial Ca/Si ratios from 0.93 to 1.05, adjusted by the WIFD content. The compressive strength of both SF and NS-modified samples follows a similar trend, where a higher WIFD content induces a higher Ca/Si ratio, subsequently resulting in reduced mechanical strength. This trend can be attributed to the fact

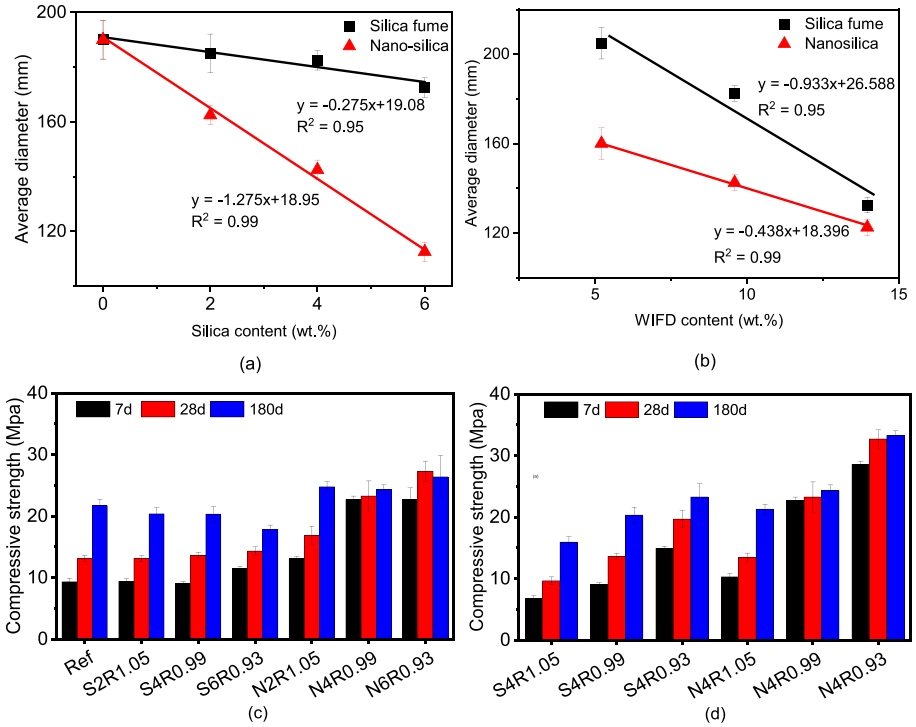

Fig. 1. Spread flow diameter of the mixture with different (a) silica content and (b) WIFD content, 7 d, 28 d and 180 d compressive strength of the mixture with different (c) silica content (0—6%) and (d) initial Ca/Si ratio (1.05, 0.99 and 0.93).

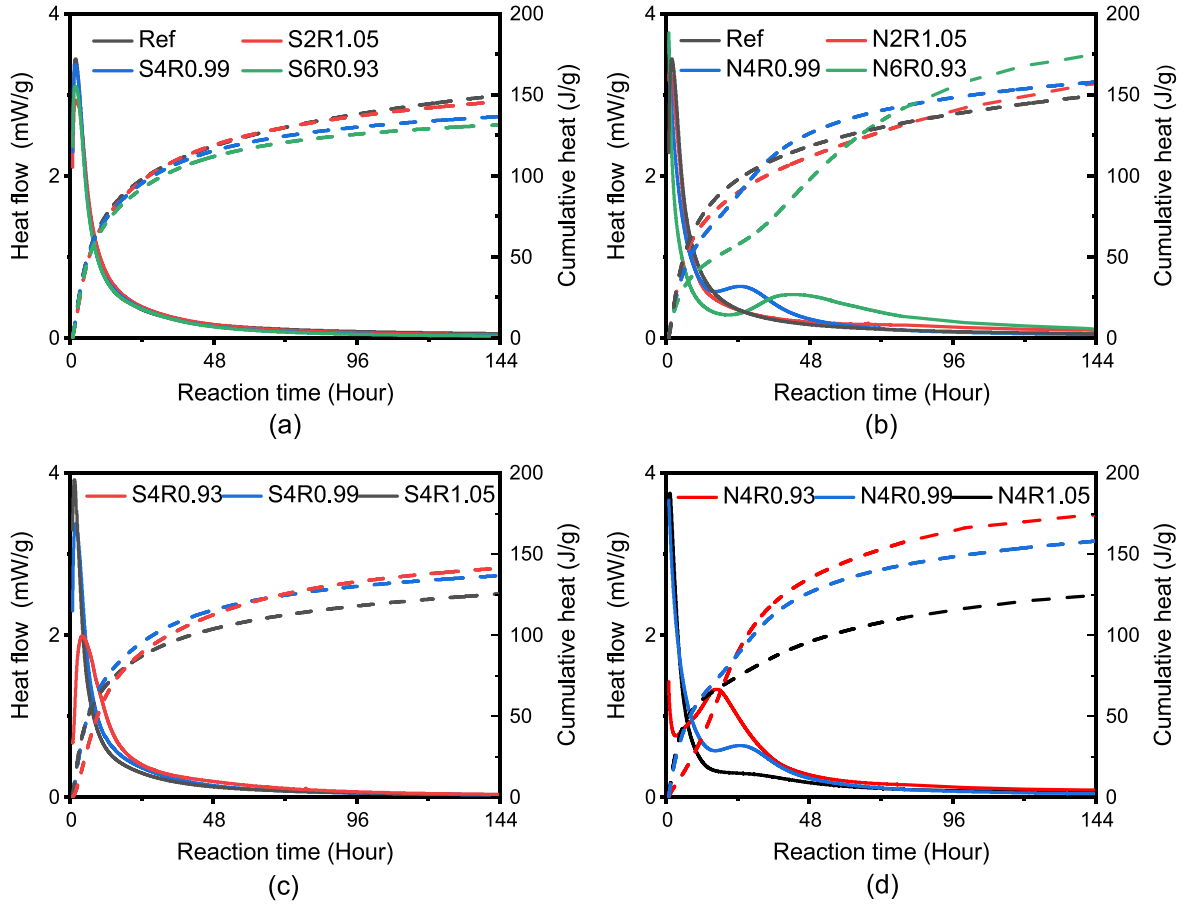

Fig. 2. Heat release of the binder with different silica source replacement from 2% to 6% by mass (a: SF, b: NS); heat release of the binder with 4 % silica replacement at different Ca/Si mole ratios (c: SF, d. NS).

that WIFD is a less reactive pozzolanic material compared to GGBFS, and the decreased workability of the binder leads to a more porous matrix structure. However, noteworthy differences emerge between the NS-modified and the SF-modified samples. The NS-modified samples show higher compressive strength than those containing silica fume at an equivalent Ca/Si ratio, indicating that NS exhibits greater reactivity than SF and contributes to the activation process together with WIFD and GGBFS.

In total, the 28 d compressive strength of all samples ranged from 10.1 to 33.5 MPa. It is crucial to highlight that the compressive strengths of most current formulations are lower than that of OPC. Consequently, attaining further improvements in strength is essential to demonstrate its potential as a cement substitute. Potential strategies for enhancing strength involve optimizing sodium carbonate dosage and adjusting the water-binder ratio. However, these efforts are beyond the scope of the current research objectives and will be continued in future investigations.

3.2. Reaction kinetics

Fig. 2 **(a)** and Fig. 2 **(b)** show the effect of the SF and NS dosage on the reaction process of the blended binder within 7 d. The dosage of SF has a negligible influence on the reaction process, as observed in the heat flow curves. It takes nearly 2 h for all SF-modified groups to reach the peaks of heat flow, indicative of the formation of reaction products (Ke et al., 2016; Shi and Day, 1995). Furthermore, only a slight decrease in cumulative heat of the binder is observed with increasing SF content, e.g., 150.1 J/g in the group Ref while it is 131.7 J/g in the 6 % SF-modified paste (S6R0.93). This reduction is attributed to the overall decrease in GGBFS content resulting from the incorporation of SF.

The NS-modified binders show different heat flow curves in Fig. 2 **(b)**. The dosage of NS results in a delayed reaction process, as evidenced by the exothermic peak occurring at different times: 1.1 h for N2R1.05, 24.5 h for N4R0.99, and 40.8 h for N6R0.93. Its intensity decreases with higher NS content, in line with findings from a previous study (Gao et al., 2017a), which is attributed to an increased activator modulus (Krizan and Zivanovic, 2002). The incorporation of NS increases the silicate content of the mortar, thereby correspondingly decreasing the pH value (Criado et al., 2008). This change in pH impacts the silicate equilibrium, affecting the alkalinity of the reaction solution. Hence, the dissolution of the silicates from GGBFS is delayed, extending the reaction time of the binder. However, the extra NS in the binder promotes higher cumulative heat. The increased reactive silicate content provided by NS contributes to the polymerization reaction, releasing more reaction heat. In general, the silicate source determines the effect on the reaction process based on the reaction degree of the added silicate. When the paste is modified with SF, no further chemical interaction occurs. SF acts as a physical filler during the reaction, whereas NS contributes more soluble silicate resulting in a lower pH (See the supplementary **Figure S3**) and a reduced reactivity of GGBFS during the initial stages. Nevertheless, the portlandite in WIFD can be more extensively combined with NS and a higher content of polymerized C-(A)-S-H can be formed.

Fig. 2 **(c)** and Fig. 2 **(d)** illustrate the heat evolution rates and cumulative heat of the mixtures with different initial Ca/Si ratios. When the Ca/Si ratio increases in pastes modified with varying sources of silicate, the cumulative heat decreases due to the lower proportion of GGBFS in the mixture, associated with the pozzolanic reaction. In the SF-modified paste, the peak of heat evolution appears after 3.8 h with a Ca/Si ratio of 0.93. As the Ca/Si ratio increases to 1.05, this peak shifts to 1.5 h with higher intensity. The duration of the main hydration reaction decreases with more incorporated WIFD due to the reduction of the overall content of GGBFS and increased portlandite content. Conversely, in the NS-modified paste, NS significantly promotes the formation of gels, providing nucleation sites for subsequent hydration products during the reaction (Rupasinghe et al., 2017). In summary, the present work confirms the adverse effect of solid waste addition on the reaction process. The decrease in cumulative heat developed upon the WIFD supplement is also consistent with the reduction in compressive strength.

3.3. Phase assemblage analysis

Fig. 3 **(a)** shows the XRD patterns of the 28 d paste samples prepared with different dosages of SF and NS. In the group Ref, the major crystalline phases identified were calcite (PDF#72–1937), hydrotalcite (PDF#89–0460), $Ca(OH)_2$ (PDF#87–0673), and hemicarboaluminate (PDF#41–0221), in agreement with previous studies on the sodium carbonate-activated slag (Ismail et al., 2014; Ke et al., 2016). The broad hump around 32-38° indicates the presence of poorly crystallized C-(A)-S-H gel (Gao et al., 2015c; Yang et al., 2012), though not distinctly marked in the XRD pattern due to overlap with calcite. This gel plays a significant role in strength development for alkali-activated materials. Notably, a portion of $Ca(OH)_2$ and calcite may originate from the raw WIFD. Xuan et al. (Ling et al., 2021) revealed that the calcite in WIFD contributes to the formation of hemicarboaluminate. Similar findings were observed in the study of a limestone-modified slag paste (De Weerdt et al., 2011; Gao et al., 2015c). The incorporation of SF (S2R1.05, S4R0.99, S6R0.93) slightly affects the intensity of hemicarboaluminate, hydrotalcite and $Ca(OH)_2$, attributed to different relative contents of raw material in each mixture. The decreased intensity of $Ca(OH)_2$ in both the SF and NS-modified paste could be attributed to the pozzolanic reaction. On the other hand, when preparing paste with NS (N2R1.05, N4R0.99, N6R0.93), the peaks of hemicarboaluminate are absent. This absence can be attributed to NS consuming more Ca^{2+} ions for the formation of C-(A)-S-H gels, resulting in an insufficient Ca^{2+} ions content. Additionally, more Al^{3+} ions are incorporated into the additional C-(A)-S-H gels that form. Nonetheless, identifying an increase in C-(A)-S-H gels content solely through XRD patterns proves challenging. Therefore, the corresponding conclusion will be further validated later in the analysis of TG-DTG results. The effect of initial Ca/Si ratios on the reaction products is illustrated in Fig. 3 **(b)**. In the SF-modified paste, the formation of hemicarboaluminate is significantly affected by the Ca/Si ratio. When the Ca/Si is higher than 0.93, the pore solution attains a sufficient Ca^{2+} concentration to facilitate the hemicarboaluminate formation, evident from the increased peak intensities. Conversely, lower peaks of hemicarboaluminate are observed in all NS-modified pastes, as NS consumes higher amounts of Ca^{2+} and Al^{3+} ions in the pore solution to form the C-(A)-S-H gel.

Fig. 3 **(c)** shows the infrared spectra of the 28 d samples prepared with different dosages of SF and NS. The addition of SF and NS mainly affects the position of the band around 950 cm^{-1}, assigned to the asymmetric stretching mode of the Si-O-T (T = tetrahedral Si or Al) bonds in the C-(A)-S-H gel (Bernal et al., 2011; Gao et al., 2015c; García Lodeiro et al., 2009). This band shifts toward a higher frequency with increasing SF or NS in the mixture, indicating enhanced polymerization of the silicate chains (Yu et al., 1999). The broad bands around 3405 cm^{-1} and 1638 cm^{-1} correspond to the stretching and bending vibration of the H-O–H bond, respectively. These resonances are from the bound water or interlayer water in the C-(A)-S-H gel, hydrotalcite and hemicarboaluminate (Ismail et al., 2014; Yu et al., 1999). The increased intensities of these bonds in SF-modified pastes are mainly attributed to the formation of hemicarboaluminate, absent in NS-modified samples as indicated in the earlier XRD results. The adsorption peaks at 1416 cm^{-1} and 873 cm^{-1} represent the vibration of $\nu3$ [CO_3^{2-}] and $\nu2$ [CO_3^{2-}] (García Lodeiro et al., 2009), respectively, which may originate from the calcite, hydrotalcite and hemicarboaluminate. Fig. 3 **(d)** shows the FT-IR spectra of the 28 d paste samples with 4 % NS or SF. Decreasing the WIFD content and lowering the initial Ca/Si ratio from 1.05 to 0.93 leads to a shift of the main peak around 946 cm^{-1} to higher wavenumber both in NS-modified and SF-modified samples. This shift indicates progressive polymerization of the silicate chains, highlighting the influence of dissolved Ca^{2+} ions from WIFD on the formation of C-(A)-S-H gel. The

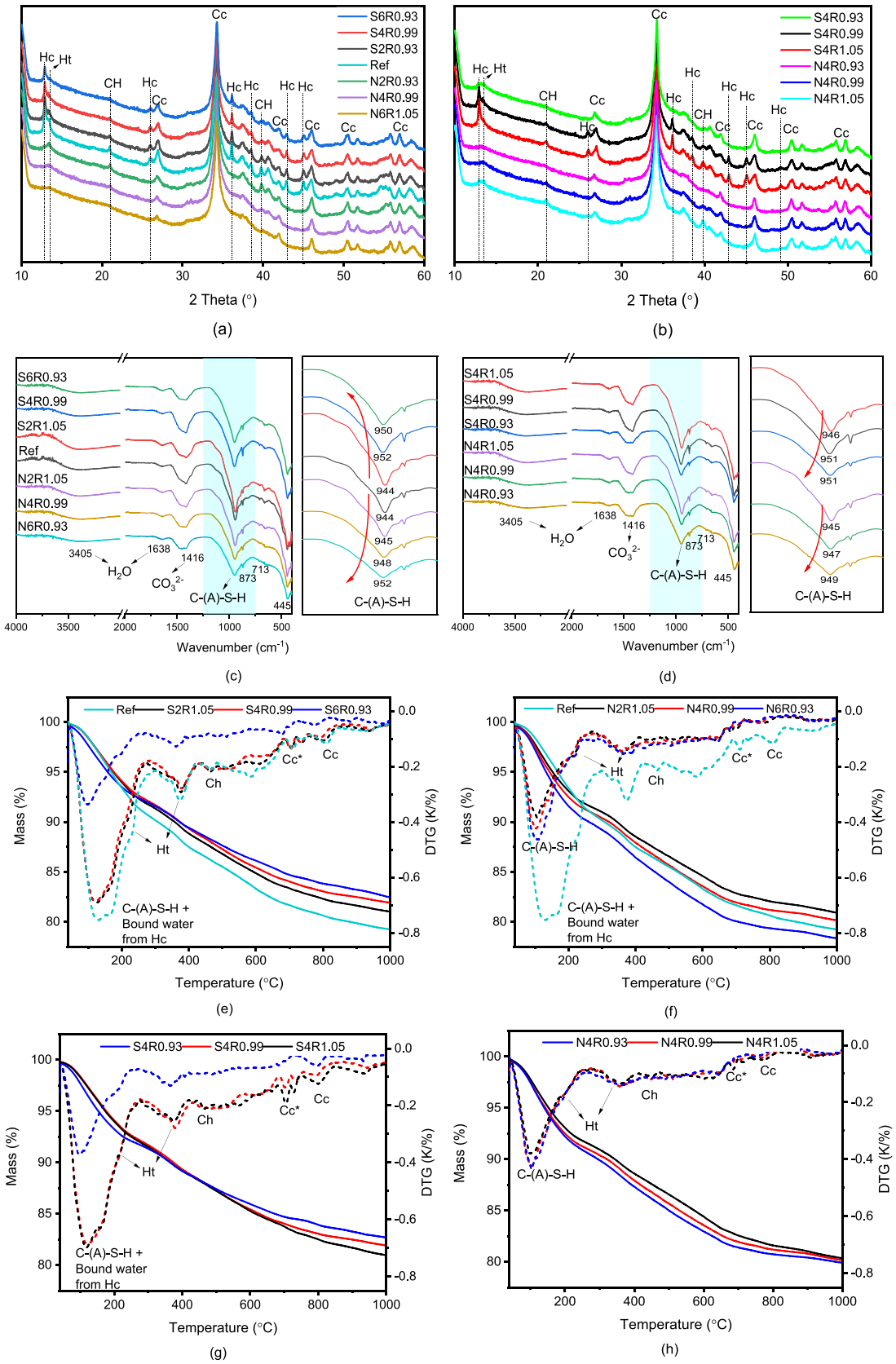

Fig. 3. XRD patterns (a-b) and FT-IR (c-d) of the 28 d paste samples prepared with (a and c) different dosages of silica additives, (b and d) 4 % silica replacement at different Ca/Si mole ratios (Hc-Hemicarboaluminate, Ht-Hydrotalcite, CH-$Ca(OH)_2$, Cc-Calcite); (e-h) TG and DTG curves of the 28 d paste samples with different dosages of silica additives and 4 % silica additives at different Ca/Si molar ratios (e and g: SF; f and h. NS).

degree of polymerization of the gels correlates with the proportion of the WIFD in the mixture.

The thermal analysis of the 28 d paste samples modified with different dosages of SF or NS is presented in Fig. 3 **(e)** and Fig. 3 **(f)**. All the samples were dried at 45 °C before the TG test, rendering the residual free water in the paste negligible. In the group Ref, a remarkable mass loss occurs around 140 °C, attributed to the dehydration of several reaction products, including the C-(A)-S-H gel (Abdalqader et al., 2019), hemicarboaluminate (Fernández et al., 2018; Lothenbach et al., 2008), and hydrotalcite (Crosby et al., 2014; Focke et al., 2009). Upon modifying the paste with SF, the mass loss caused by the dehydration of these minerals decreases, indicating a lower content of reaction products due to different proportions of initial materials. On the other hand, the DTG curves of all NS modified samples show notably smaller peaks for the dehydration of these minerals than the group Ref. This is because the addition of NS inhibits the formation of hemicarboaluminate according to the XRD analysis. Consequently, the primary mass loss in NS-modified paste is attributed to the dehydration of C-(A)-S-H. It is noteworthy that an augmented mass loss is observed with an increase in NS content, implying greater incorporation of free water into the gel products during the hydration process. Simultaneously, the peak associated with Ca $(OH)_2$ decomposition confirms that NS promotes the consumption of WIFD and the consequent formation of additional C-(A)-S-H gel, consistent with the increased cumulative heat and enhanced compressive strength.

Fig. 3 **(g)** and Fig. 3 **(h)** present the TG and DTG curves of the 28 d paste modified with 4 % SF or NS. The mass loss due to the dehydration of bound water around 140 °C is influenced by the initial Ca/Si ratio. A higher Ca/Si ratio induces the formation of hemicarboaluminate in SF-modified samples, which contains a higher amount of bound water. When the Ca/Si ratio is above 0.99, the DTG curves of S4R0.99 and S4R1.05 are similar, indicating the presence of sufficient Ca^{2+} ions in the solution. However, the initial Ca/Si ratio shows a different effect on the reaction products in the NS-modified paste. This difference can be attributed to the heightened concentration of reactive silicate content introduced by NS, which subsequently results in the consumption of Ca^{2+} ions during the formation of C-(A)-S-H gels. Therefore, an increased Ca/Si ratio contributes to the development of a less polymerized structure, accompanied by a reduction in the amount of bound water.

3.4. Gel pore characterization

The pore size distribution (2 – 110 nm) and specific surface area of the samples are shown in Fig. 4. The addition of SF or NS influences the formation of C-(A)-S-H gel, which constitutes a porous gel with a high specific surface area. Generally, the voids within the cementitious system are classified as interlayer space (<0.5 nm), gel pores (0.5 – 10 nm), capillary pores (10 nm – 50 μm) and air voids (>50 μm) (S. Y. Wang et al., 2020b). The gel pores and capillary pores exhibit sensitivity to the different silica sources (Fig. 4 **(a)**). The use of SF leads to a negligible difference in the gel pores, while reducing the volume of capillary pores and increasing the surface area from 11.0 to 12.1 m^2/g. This illustrates the relatively lower pozzolanic reactivity and filler effect of SF. In contrast, when NS is utilized in paste preparation, the volume of the larger capillary pores (>50 nm) decreases and the volume of the smaller capillary pores (10 – 50 nm) increases, accompanied by a higher surface area of 15.6 m^2/g. This is because the larger capillary pores are filled with the newly formed gel products and transformed into smaller pores. Similar results were reported for a NS-modified cement paste (Hou et al., 2015), where the creation of a more porous bulk structure due to the blocking of ions diffusion from the unreacted cement particles by the gel products was observed. However, the strength and permeability characteristics of the blended binders are determined by the capillary pores larger than 50 nm (Mehta and Monteiro, 2006). Therefore, in comparison to SF, the greater reduction in the volume of the larger capillary pores achieved by NS contributes to a better 28 d compressive strength.

Since the different initial Ca/Si ratios result in different hydration products, the pore size distribution in the SF and NS-modified samples is clarified in Fig. 4 **(b)** and **(c)**, respectively. The higher Ca/Si ratio induced by WIFD addition in both reaction systems leads to an increased volume of capillary pores, aligning with the reduced compressive

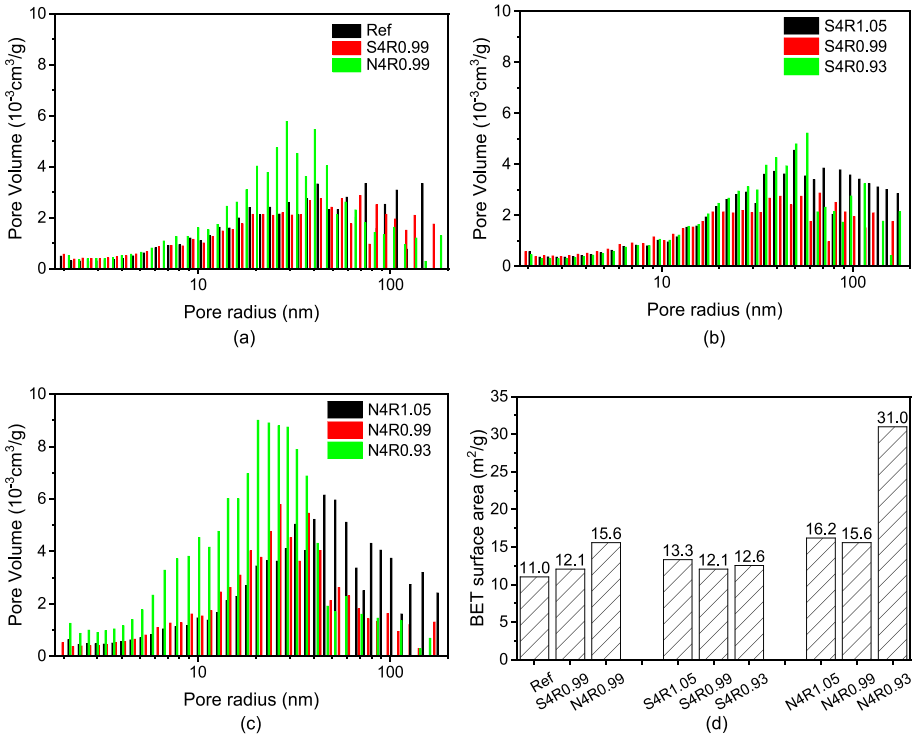

Fig. 4. (a-c) BJH pore size distributions and (d) BET surface area of 28 d samples.

strength detectable in Fig. 1. Actually, when the Ca/Si ratio increases from 0.99 to 1.05, the BET surface area for both S4R1.05 and N4R1.05 increases, suggesting that more $Ca(OH)_2$ from WIFD is beneficial for the pozzolanic reaction of SiO_2 and enhances the formation of C-(A)-S-H gel. However, it is insufficient to compensate for the reduction of the overall hydrated phase caused by replacing GGBFS with WIFD (Rupasinghe et al., 2017). When the Ca/Si ratio is lowered by the decreased WIFD content, this leads to a reduction in the volume of the smaller capillary pores in S4R0.93 and gel pores in N4R0.93. Hence, the inclusion of silica additives significantly influences the pore structure of the blends.

3.5. Microstructure and gel composition

SF and NS-modified pastes show differences in the formation of hemicarboaluminate and polymerization degree of the gels, subsequently influencing the composition and structure of C-(A)-S-H gel. Hence, the Ca/Si and Al/Si ratios of the gel products are quantitatively evaluated through BSE-EDX analysis. Supplementary **Figure S4** shows a typical BSE image from group Ref after 28 d curing. Within the image, unreacted slag grains and their surrounding reaction rims can be clearly distinguished, along with large pores and calcite. The regions characterized by darker greyscale values correspond to the reacted slag fines, as reported elsewhere (Walling et al., 2018).

To verify the composition of the reaction products, 100 EDX analysis spots (excluding the unreacted slag, calcite and pores) were randomly collected for each sample. The compositional analysis of the samples prepared both with and without SF and NS is shown in Fig. 5. Regardless of the silica additives, a distinct correlation between the Mg/Si and Al/Si ratios is evident in Fig. 5 **(a),** confirming the presence of a hydrotalcite-type phase with an approximate Mg/Al molar ratio of 1.9. Similar Mg/Al ratios for hydrotalcite have been revealed in previous studies (Walling et al., 2018; Ye et al., 2019). However, some spots in Ref and S4R0.99 show notably lower Mg/Al ratios, attributable to the inclusion of hemicarboaluminate ($C_4A\overline{C}_{0.5}H_{12}$) within the bulk matrix. Furthermore, an Al/Si ratio of approximately 0.23 is observed when Mg/Si = 0, suggesting an approximated Al/Si ratio within the C-(A)-S-H gels, in agreement with the Al/Si ratio depicted in Fig. 5 **(b)**. This demonstrates a consistent Al(IV) substitution ratio for Si in C-(A)-S-H gel regardless of the silica additives (Richardson, 2008). Likewise, the presence of $C_4A\overline{C}_{0.5}H_{12}$ in Ref and S4R0.99 leads to a higher Al/Mg ratio in some spots.

Fig. 5 **(c)** shows the Ca/Si ratio within the C-(A)-S-H gels under the influence of SF and NS modifications. Despite the presence of $C_4A\overline{C}_{0.5}H_{12}$ in the Ref, resulting in a higher Ca concentration, the Ca/Si ratio in the C-(A)-S-H gel remains approximately 1.25. The relatively low Ca/Si ratio in alkali-activated slag indicates the presence of a C-S-H

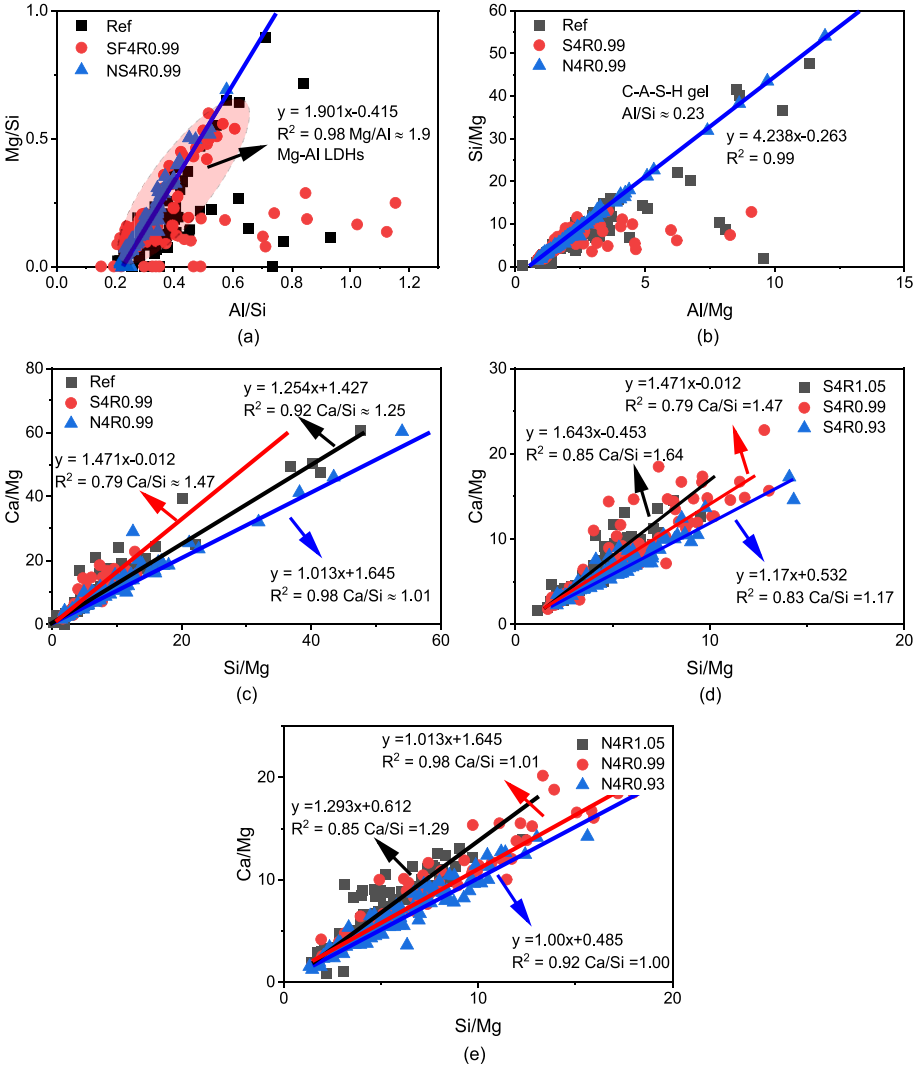

Fig. 5. Compositional plots of the different spots measured (100 spots) in the 28 d samples with molar ratios of (a) Mg/Si and Al/Si; (b) Si/Mg and Al/Mg; (c-e) Ca/Mg and Si/Mg (The trend lines are fit to the measured spots, and the slope of each line is calculated which represents the Mg/Al ratio in (a), Al/Si ratio in (b), and Ca/Si ratio in (c-e)).

(I) gel structure (Shi et al., 2003). Contrary to expectations for a pozzolanic reaction, the SF-modified samples, as illustrated by the red curve in Fig. 5 **(c)**, do not exhibit a significant reduction in the Ca/Si ratio, implying the low reactivity of SF. On the other hand, the addition of NS reduces the Ca/Si ratio within the C-(A)-S-H gels to 1.01. This reduction affirms an enhanced polymerization degree of the C-(A)-S-H gel with longer silicate chains, attributed to improved Q^2 content by NS (Kong et al., 2019), which is coherent with the findings from the FT-IR results in Fig. 3 **(c)**.

The actual Ca/Si ratio of the formed C-(A)-S-H gel within each mixture, with different dosages of WIFD incorporated into the SF-modified and NS-modified samples, are presented in Fig. 5 **(d)** and Fig. 5 **(e)**, respectively. The actual Ca/Si ratio is higher than the initial Ca/Si ratio provided in Table 1, e.g., the Ca/Si ratio is 1.64, 1.47 and 1.17 in SF-modified mixtures. This phenomenon could be attributed to the unreacted GGBFS and the release of more reactive Ca^{2+} from WIFD. Moreover, the addition of NS leads to the development of a C-(A)-S-H gel with a lower actual Ca/Si ratio compared to the samples modified with SF, indicating that NS promotes the hydration process of WIFD within the matrix.

3.6. Carbonation depths and rate

The carbonation front is indicated by phenolphthalein for each mixture, as shown in Supplementary **Figure S5**. The diffusion of CO_2 in alkali-activated materials lowers the pH value of the pore solution (Shi et al., 2003, 2018a) and decalcifies calcium-bearing phases such as the C-(A)-S-H gels (Bernal et al., 2015, 2013; Shi et al., 2018a). The magenta in the centre represents the uncarbonated parts. It is evident that increased carbonation occurs in the mortar prepared with NS (N4R0.99 > S4R0.99 > Ref) after 8 d accelerated carbonation. Upon incorporation of varying dosages of WIFD to adjust the initial Ca/Si ratio, distinct carbonation depths are observed in the SF-modified and NS-modified samples, as illustrated in S4R1.05–0.93 and N4R1.05–0.93. Notably, while the uncarbonated area increases with a lower Ca/Si ratio in SF-modified samples, it initially decreases in NS-modified samples with a reduction in the Ca/Si ratio, but increases when the Ca/Si ratio is further lowered.

To assess the carbonation rate of various samples, the evolution of carbonation depth in the mortar samples is presented in Supplementary **Figure S6**. The linear correlation between carbonation depth and the square root of exposure time confirms the diffusion-controlled process. Linear fitting is performed for each mixture, excluding the full carbonation point (20 mm), and the slope of each fitted line is considered as the carbonation rate in Table 2. The resistance to carbonation shows variation between the two silica additives. In comparison to the group Ref, the addition of 2 % SF (S2R1.05) can reduce the carbonation rate. However, a further increase in SF content leads to an accelerated diffusion of CO_2. Conversely, among the NS-modified samples, higher NS content improves carbonation resistance (N2R1.05, N4R0.99, N6R0.93). As the incorporation of silica additives can enhance the mechanical properties of the blends, an improvement in carbonation resistance was expected, particularly for mixtures modified with NS. However, NS-modified samples exhibit a faster carbonation rate compared to group Ref. Several potential reasons contribute to this phenomenon: a) the lower workability of NS-modified samples introduces more air voids in the matrix; b) while NS promotes the gel formation, the matrix retains less portlandite, allowing diffused CO_2 to react directly with the gels instead of carbonating portlandite first; c) C-(A)-S-H gels formed in NS-modified samples show a lower Ca/Si ratio, resulting in decreased CO_2 binding capacities; d) the higher BET surface area of gel products in NS-modified samples facilitates CO_2 diffusion; e) more free water remaining in the NS-modified sample induces higher internal relative humidity and accelerates the penetration of CO_2 (El-Turki et al., 2007), whereas more free water in Ref samples is bounded into the formation of hemicarboaluminate, hydrotalcite and C-(A)-S-H gel. With further hydration processes, the consumption of free water also contributes to the formation of voids.

On the other hand, the different initial Ca/Si ratio of raw material induces various carbonation responses in the mortars. In the SF-modified samples, as the proportion of WIFD increases from S4R0.93 to S4R1.05 in the mixture, the carbonation rate decreases, indicating that WIFD retards the carbonation process. A similar trend is observed in N4R1.05 when compared with N4R0.99. Notably, N4R0.93 shows the best carbonation resistance among all NS-modified mixtures, attributed to the increased gel products that fill the voids, reduce the pore size of the matrix, and consequently slow down the diffusion of CO_2.

In conclusion, the carbonation behaviour of the blended binder was studied by varying the content of NS, SF, and WIFD. Among the groups studied, S2R1.05 and N4R0.93 demonstrate better carbonation resistance compared to the group Ref. Considering the aim of optimizing WIFD waste utilization, formulations such as S2R1.05 are recommended for blend preparation.

4. Discussions

4.1. Preliminary study on CO_2 emissions and cost of the blended binder

The development of AAMs is primarily motivated by the need to reduce the adverse environmental impacts of cement production and usage, particularly in terms of CO_2 emission reduction (Colangelo et al., 2021). Hence, the embodied CO_2 of the mixes developed in this work was preliminary estimated and compared with other types of binder systems (Gao et al., 2017a; Sumajouw et al., 2007; Weil et al., 2009), along with a cost analysis of raw materials. CO_2 emissions (kg CO_2/ton) and overall cost (€/ton) of the mix were calculated by multiplying the mass of each ingredient (in 1 m^3) by its CO_2 coefficient and price, respectively. The CO_2 emission and price indicators of each ingredient were obtained from the literature (Adesina, 2021; Collins, 2010; Flower and Sanjayan, 2007; Gao et al., 2017a; García, 2014; Gholizadeh-Vayghan et al., 2021; Heede and Belie, 2012; Valente et al., 2022; Yuan et al., 2017a), as presented in **Supplementary Text S4**.

The CO_2 emission and the cost of S4R0.99 and N4R0.99 from the current study and other types of concrete are presented in Supplementary **Figure S7.** It confirms the highest CO_2 emission in OPC concrete, mainly attributed to the usage of CEM I. Reduction of CO_2 emissions is achieved in different AAM-based concrete. Notably, activators may significantly contribute to CO_2 emissions in sodium silicate or sodium hydroxide activated-materials (Flower and Sanjayan, 2007), as evidenced in GGBFS/CFA-SS, GGBFS/CFA-NS and CFA-SS in Supplementary **Figure S7**. Lower CO_2 emissions are achieved by using sodium carbonate as an activator in S4R0.99 and N4R0.99. Additionally, sodium

Table 2
The carbonation rate of each mixture by linear fitting analysis of **Supplementary Figure S6** (Note: the full carbonation points are excluded during the fitting, the slope is then considered as the carbonation rate, and the fitting results are presented in **Supplementary Figure S6**).

Group ID	Ref	S2R 1.05	S4R 1.05	S4R 0.99	S4R 0.93	S6R 0.93	N2R 1.05	N4R 1.05	N4R 0.99	N4R 0.93	N6R 0.93
Carbonat-ion rate ($mm/d^{1/2}$)	5.212	4.938	5.639	5.686	5.807	5.666	7.439	5.745	7.390	4.915	5.456
R-Square	0.998	0.999	0.995	0.999	0.993	0.998	0.991	0.993	0.999	0.998	0.968

carbonate is cheaper than sodium silicate or sodium hydroxide-based activators, reducing the cost of the S/N4R0.99.

Generally, the use of NS will significantly increase energy consumption and cost in the production of AAMs. When compared with SF-modified samples, a higher CO_2 footprint is confirmed in NS-modified samples. Notably, the NS used in this study was derived from olivine. Previous research conducted by our group has revealed its CO_2 footprint and cost through laboratory and bench-scale testing (Gao et al., 2017a; García, 2014). When compared to the conventional production of NS using waterglass, the cost of raw materials can be reduced from 2084 €/tone to 941€/tone, and the CO_2 emission can be lowered from 8800 kg/tone to 461 kg/tone (García, 2014; Uddin et al., 2019). Overall, the contribution of NS to CO_2 emission is relatively lower than that of other ingredients in the concrete. Therefore, improving the integration of WIFD in the sodium carbonate-activated GGBFS with NS or SF is acceptable with lower costs and a reduced carbon footprint.

4.2. Reaction mechanism of SF and NS

The present work reveals various effects of SF and NS on the reaction process and overall performance of the blends. The schematic diagram of the proposed mechanism is presented in Fig. 6. The pozzolanic reaction of silica additives can be considered a major factor that improves the gel production and, thereby, the mechanical properties of the blends (Hou et al., 2015). However, a significant promotion of gel formation is evident exclusively in blends containing NS, which explains the remarkable enhancement of the mechanical properties of the blends in this case. The formed C-(A)-S-H gel shows a lower Ca/Si ratio and higher polymerization, indicating a longer aluminosilicate tetrahedra chain and enhanced gel density (Myers et al., 2015). Notably, the improved compressive strength of the NS-modified blends does not guarantee a better carbonation resistance of the matrix. SF slightly contributes to the mechanical properties of the blends as fillers, and the resulting C-(A)-S-H gel has a higher Ca/Si ratio. Sevelsted and Skibsted have documented a decline in carbonation rate with an elevated Ca/Si ratio of C-S-H gel (Sevelsted and Skibsted, 2015). A similar improvement in carbonation resistance is achieved within the group with 2 % SF addition. To sum up, SF and NS contribute to the mechanical properties from different physicochemical mechanisms, making it feasible to optimize the performance of WIFD-sodium carbonate-activated materials to align with specific construction demands. However, further advancements in mechanical attributes are imperative for these materials serve a viable cement alternative, given that the compressive strength of most modified samples remains below the 32.5 MPa at 28 d.

5. Conclusions

The effect of silica fume (SF) and nano-silica (NS) on the workability, mechanical properties, reaction kinetics, phase and gel composition, microstructure and carbonation resistance of the novel WIFD-combined binder is intensively investigated in the present work, along with the evaluated CO_2 footprint and cost analysis. The following conclusions can be drawn based on the obtained results:

1. SF increases the compressive strength of the blended mortar slightly at early ages due to the filler effect but decreases at longer ages due to a lower amount of hydration products, whereas NS enhanced the compressive strength at all ages due to better pozzolanic reactivity and improved formation of C-(A)-S-H gels that refine the pore structure.
2. NS promotes the consumption of WIFD in the matrix and enhances the cumulative heat released due to the improved gel formation in the blends. However, it retards the reaction process, as a result of the reduced pH value of the pore solution due to the pozzolanic reaction.
3. The main reaction products of the WIFD-sodium carbonate-activated binders are C-(A)-S-H gel, hemicarboaluminate ($C_4A\,\overline{C}_{0.5}H_{12}$), hydrotalcite (Mg-Al LDHs) and calcite. The addition of NS inhibits the formation of $C_4A\,\overline{C}_{0.5}H_{12}$ and Mg-Al LDHs by the consumption of Ca^{2+} and Al^{3+} in gel formation.
4. 4 % NS leads to a relatively lower Ca/Si ratio of 1.01 in C-(A)-S-H gels and induces a higher polymerization degree of silicate chains, whereas no significant influence of SF in gel composition with a relatively higher Ca/Si ratio of 1.47. The substitution of Al in silica chains is approximately 0.23 regardless of the silica additives.
5. Though NS enhances the mechanical properties of the blends, it also induces a lower carbonation resistance of the matrix. Instead, using 2 % SF and WIFD is beneficial to improve the carbonation resistance, which can be optimized as the S2R1.05.

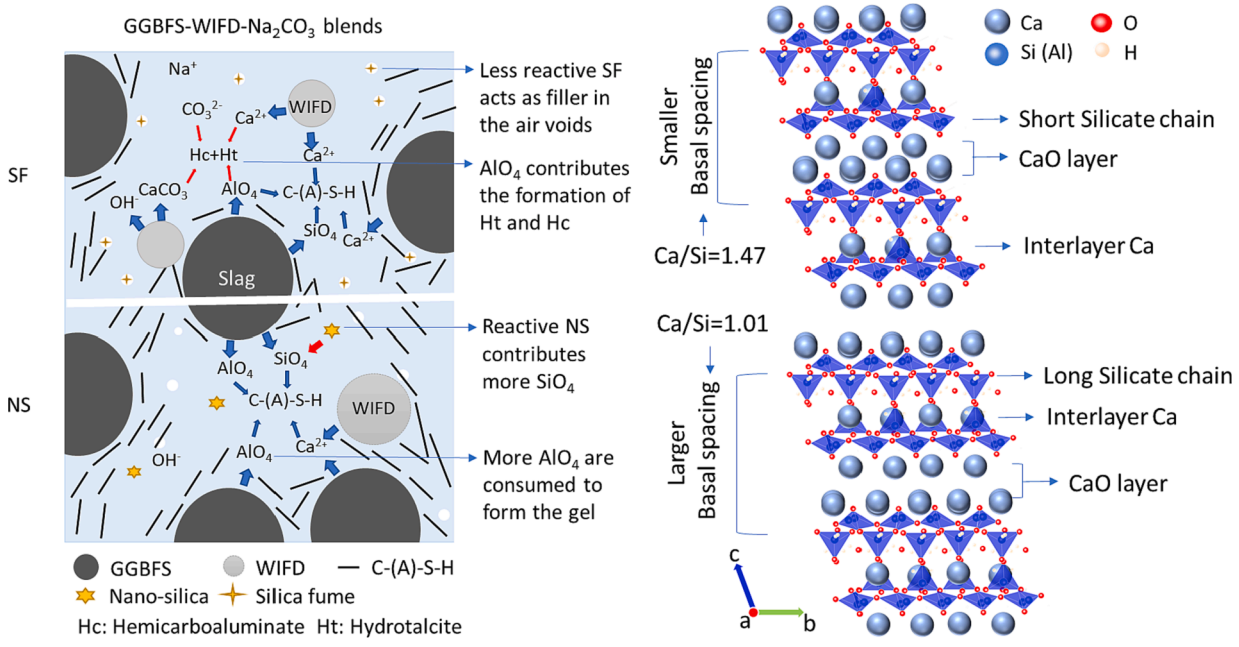

Fig. 6. Schematics of the role of nano-silica and silica fume on the activation process of the GGBFS-WIFD-Na_2CO_3 system.

6. The designed WIFD-sodium carbonate-activated slag concrete offers advantages in terms of reducing CO_2 emissions and the cost of raw materials when compared to the OPC system and sodium silicate/hydroxide-activated system. In addition, the work provides an alternative management practice for air pollution control residues.
7. The findings presented in this paper are confined to the examination of the compressive strength, reaction process and products, microstructure and carbonation behaviour of GGBFS-WIFD-Na_2CO_3 system. While the compressive strength requires further enhancements, other aspects such as shrinkage behaviour and durability require comprehensive elucidation and analysis before considering the implementation of this process on a bench or industrial scale.

Declaration of competing interest

The authors declare that they have no known competing financial interests or personal relationships that could have appeared to influence the work reported in this paper.

Data availability

Data will be made available on request.

Acknowledgements

This work was supported by the funding of the China Scholarship Council (No. 201906950015) and Eindhoven University of Technology. The authors would like to thank Euro Trust Management for the supply of waste incineration filter dust.

Appendix A. Supplementary data

Supplementary data to this article can be found online at https://doi.org/10.1016/j.wasman.2024.01.028.

References

Abdalqader, A., Jin, F., Al-Tabbaa, A., 2019. Performance of magnesia-modified sodium carbonate-activated slag/fly ash concrete. Cem. Concr. Compos. 103, 160–174. https://doi.org/10.1016/j.cemconcomp.2019.05.007.

Adesina, A., 2021. Performance and sustainability overview of sodium carbonate activated slag materials cured at ambient temperature. Resour. Environ. Sustain. 3, 100016 https://doi.org/10.1016/J.RESENV.2021.100016.

Ben Haha, M., Le Saout, G., Winnefeld, F., Lothenbach, B., 2011. Influence of activator type on hydration kinetics, hydrate assemblage and microstructural development of alkali activated blast-furnace slags. Cem. Concr. Res. 41, 301–310. https://doi.org/10.1016/j.cemconres.2010.11.016.

Bernal, S.A., Provis, J.L., Mejı, R., Deventer, J.S.J. Van, 2015. Accelerated carbonation testing of alkali-activated slag / metakaolin blended concretes : effect of exposure conditions 653–669. 10.1617/s11527-014-0289-4.

Bernal, S.A., Provis, J.L., Rose, V., Mejía De Gutierrez, R., 2011. Evolution of binder structure in sodium silicate-activated slag-metakaolin blends. Cem. Concr. Compos. 33, 46–54. https://doi.org/10.1016/j.cemconcomp.2010.09.004.

Bernal, S.A., Mejía De Gutiérrez, R., Provis, J.L., 2012a. Engineering and durability properties of concretes based on alkali-activated granulated blast furnace slag/metakaolin blends. Constr. Build. Mater. 33, 99–108. https://doi.org/10.1016/J.CONBUILDMAT.2012.01.017.

Bernal, S.A., Provis, J.L., Brice, D.G., Kilcullen, A., Duxson, P., Van Deventer, J.S.J., 2012b. Accelerated carbonation testing of alkali-activated binders significantly underestimates service life: The role of pore solution chemistry. Cem. Concr. Res. 42, 1317–1326. https://doi.org/10.1016/J.CEMCONRES.2012.07.002.

Bernal, S.A., Provis, J.L., Walkley, B., San Nicolas, R., Gehman, J.D., Brice, D.G., Kilcullen, A.R., Duxson, P., Van Deventer, J.S.J., 2013. Gel nanostructure in alkali-activated binders based on slag and fly ash, and effects of accelerated carbonation. Cem. Concr. Res. 53, 127–144. https://doi.org/10.1016/j.cemconres.2013.06.007.

Bernal, S.A., Provis, J.L., Myers, R.J., San Nicolas, R., van Deventer, J.S.J., 2014. Role of carbonates in the chemical evolution of sodium carbonate-activated slag binders. Mater. Struct. Constr. 48, 517–529. https://doi.org/10.1617/s11527-014-0412-6.

Brunauer, S., Emmett, P.H., Teller, E., 1938. Adsorption of Gases in Multimolecular Layers. J. Am. Chem. Soc. 60, 309–319. https://doi.org/10.1021/ja01269a023.

Cheah, C.B., Tan, L.E., Ramli, M., 2019. The engineering properties and microstructure of sodium carbonate activated fly ash/ slag blended mortars with silica fume. Compos. Part B Eng. 160, 558–572. https://doi.org/10.1016/j.compositesb.2018.12.056.

Colangelo, F., Farina, I., Travaglioni, M., Salzano, C., Cioffi, R., Petrillo, A., 2021. Eco-efficient industrial waste recycling for the manufacturing of fibre reinforced innovative geopolymer mortars: Integrated waste management and green product development through LCA. J. Clean. Prod. 312, 127777 https://doi.org/10.1016/j.jclepro.2021.127777.

Collins, F., 2010. Inclusion of carbonation during the life cycle of built and recycled concrete : influence on their carbon footprint. Int. J. Life Cycle Assess. 15, 549–556. https://doi.org/10.1007/s11367-010-0191-4.

Criado, M., Fernández-Jiménez, A., Palomo, A., Sobrados, I., Sanz, J., 2008. Effect of the SiO2/Na2O ratio on the alkali activation of fly ash. Part II: 29Si MAS-NMR Survey. Microporous Mesoporous Mater. 109, 525–534. https://doi.org/10.1016/J.MICROMESO.2007.05.062.

Crosby, S., Tran, D., Cocke, D., Duraia, E.S.M., Beall, G.W., 2014. Effect of isomorphous substitution on the thermal decomposition mechanism of hydrotalcites. Materials (basel). 7, 7048–7058. https://doi.org/10.3390/ma7107048.

De Weerdt, K., Kjellsen, K.O., Sellevold, E., Justnes, H., 2011. Synergy between fly ash and limestone powder in ternary cements. Cem. Concr. Compos. 33, 30–38. https://doi.org/10.1016/J.CEMCONCOMP.2010.09.006.

El-Turki, A., BaLL, R.J., Allen, G.C., 2007. The influence of relative humidity on structural and chemical changes during carbonation of hydraulic lime. Cem. Concr. Res. 37, 1233–1240. https://doi.org/10.1016/j.cemconres.2007.05.002.

Fernández, García Calvo, J.L., Alonso, M.C., 2018. Ordinary Portland Cement composition for the optimization of the synergies of supplementary cementitious materials of ternary binders in hydration processes. Cem. Concr. Compos. 89, 238–250. 10.1016/J.CEMCONCOMP.2017.12.016.

Flower, D.J.M., Sanjayan, J.G., 2007. Green house gas emissions due to concrete manufacture. Int. J. Life Cycle Assess. 12, 282–288. https://doi.org/10.1007/s11367-007-0327-3.

Focke, W.W., Molefe, D., Labuschagne, F.J.W., Ramjee, S., 2009. The influence of stearic acid coating on the properties of magnesium hydroxide, hydromagnesite, and hydrotalcite powders. J. Mater. Sci. 44, 6100–6109. https://doi.org/10.1007/s10853-009-3844-6.

Gao, X., Yu, Q.L., Brouwers, H.J.H., 2015a. Reaction kinetics, gel character and strength of ambient temperature cured alkali activated slag–fly ash blends. Constr. Build. Mater. 80, 105–115. https://doi.org/10.1016/J.CONBUILDMAT.2015.01.065.

Gao, X., Yu, Q.L., Brouwers, H.J.H., 2015b. Characterization of alkali activated slag–fly ash blends containing nano-silica. Constr. Build. Mater. 98, 397–406. https://doi.org/10.1016/J.CONBUILDMAT.2015.08.086.

Gao, X., Yu, Q.L., Brouwers, H.J.H., 2015c. Properties of alkali activated slag–fly ash blends with limestone addition. Cem. Concr. Compos. 59, 119–128. https://doi.org/10.1016/J.CEMCONCOMP.2015.01.007.

Gao, X., Yu, Q.L., Lazaro, A., Brouwers, H.J.H., 2017a. Investigation on a green olivine nano-silica source based activator in alkali activated slag-fly ash blends: Reaction kinetics, gel structure and carbon footprint. Cem. Concr. Res. 100, 129–139. https://doi.org/10.1016/j.cemconres.2017.06.007.

Gao, X., Yuan, B., Yu, Q.L., Brouwers, H.J.H., 2017b. Characterization and application of municipal solid waste incineration (MSWI) bottom ash and waste granite powder in alkali activated slag. J. Clean. Prod. 164, 410–419. https://doi.org/10.1016/J.JCLEPRO.2017.06.218.

Gao, X., Yao, X., Yang, T., Zhou, S., Wei, H., Zhang, Z., 2021. Calcium carbide residue as auxiliary activator for one-part sodium carbonate-activated slag cements: compressive strength, phase assemblage and environmental benefits. Constr. Build. Mater. 308, 125015 https://doi.org/10.1016/j.conbuildmat.2021.125015.

García Lodeiro, I., Macphee, D.E., Palomo, A., Fernández-Jiménez, A., 2009. Effect of alkalis on fresh C-S-H gels FTIR analysis. Cem. Concr. Res. 39, 147–153. https://doi.org/10.1016/j.cemconres.2009.01.003.

García, A.L., 2014. Nano-silica production at low temperatures from the dissolution of olivine.

Gebregziabiher, B.S., Thomas, R.J., Peethamparan, S., 2016. Temperature and activator effect on early-age reaction kinetics of alkali-activated slag binders. Constr. Build. Mater. 113, 783–793. https://doi.org/10.1016/j.conbuildmat.2016.03.098.

Gholizadeh-Vayghan, A., Nofallah, M.-H., Khaloo, A., 2021. Technoeconomic Study of Alkali-Activated Slag Concrete with a Focus on Strength, CO2 Emission, and Material Cost. J. Mater. Civ. Eng. 33, 1–12. https://doi.org/10.1061/(asce)mt.1943-5533.0003763.

Heede, P.V., Den, B., De, N., 2012. Environmental impact and life cycle assessment (LCA) of traditional and ' green' concretes : Literature review and theoretical calculations. Cem. Concr. Compos. 34, 431–442. https://doi.org/10.1016/j.cemconcomp.2012.01.004.

Hou, P., Qian, J., Cheng, X., Shah, S.P., 2015. Effects of the pozzolanic reactivity of nanoSiO2 on cement-based materials. Cem. Concr. Compos. 55, 250–258. https://doi.org/10.1016/J.CEMCONCOMP.2014.09.014.

Ismail, I., Bernal, S.A., Provis, J.L., San Nicolas, R., Hamdan, S., Van Deventer, J.S.J., 2014. Modification of phase evolution in alkali-activated blast furnace slag by the incorporation of fly ash. Cem. Concr. Compos. 45, 125–135. https://doi.org/10.1016/j.cemconcomp.2013.09.006.

Jeon, D., Jun, Y., Jeong, Y., Oh, J.E., 2015. Microstructural and strength improvements through the use of Na2CO3 in a cementless Ca(OH)2-activated Class F fly ash system. Cem. Concr. Res. 67, 215–225. https://doi.org/10.1016/j.cemconres.2014.10.001.

Kapeluszna, E., Kotwica, Ł., Różycka, A., Gołek, Ł., 2017. Incorporation of Al in C-A-S-H gels with various Ca/Si and Al/Si ratio: Microstructural and structural characteristics with DTA/TG, XRD, FTIR and TEM analysis. Constr. Build. Mater. 155, 643–653. https://doi.org/10.1016/j.conbuildmat.2017.08.091.

Ke, X., Bernal, S.A., Provis, J.L., 2016. Controlling the reaction kinetics of sodium carbonate-activated slag cements using calcined layered double hydroxides. Cem. Concr. Res. 81, 24–37. https://doi.org/10.1016/j.cemconres.2015.11.012.

Kong, D., Pan, H., Wang, L., Corr, D.J., Yang, Y., Shah, S.P., Sheng, J., 2019. Effect and mechanism of colloidal silica sol on properties and microstructure of the hardened

cement-based materials as compared to nano-silica powder with agglomerates in micron-scale. Cem. Concr. Compos. 98, 137–149. https://doi.org/10.1016/J.CEMCONCOMP.2019.02.015.
Krizan, D., Zivanovic, B., 2002. Effects of dosage and modulus of water glass on early hydration of alkali–slag cements. Cem. Concr. Res. 32, 1181–1188. https://doi.org/10.1016/S0008-8846(01)00717-7.
Lázaro García, A., 2014. Nano-silica production at low temperatures from the dissolution of olivine, PhD Thesis,. Eindhoven University of Technology. 10.6100/IR774494.
Leemann, A., Moro, F., 2017. Carbonation of concrete: the role of CO2 concentration, relative humidity and CO2 buffer capacity. Mater. Struct. Constr. 50, 1–14. https://doi.org/10.1617/s11527-016-0917-2.
Li, N., Shi, C., Zhang, Z., 2019. Understanding the roles of activators towards setting and hardening control of alkali-activated slag cement. Compos. Part B Eng. 171, 34–45. https://doi.org/10.1016/j.compositesb.2019.04.024.
Li, H., Xiao, H.G., Yuan, J., Ou, J., 2004. Microstructure of cement mortar with nano-particles. Compos. Part B Eng. 35, 185–189. https://doi.org/10.1016/S1359-8368(03)00052-0.
Ling, X., Schollbach, K., Liu, G., Brouwers, H.J.H., 2021. The utilization of waste incineration filter dust (WIFD) in sodium carbonate activated slag mortars. Constr. Build. Mater. 313, 125494 https://doi.org/10.1016/j.conbuildmat.2021.125494.
Liu, G., Florea, M.V.A., Brouwers, H.J.H., 2021. The role of recycled waste glass incorporation on the carbonation behaviour of sodium carbonate activated slag mortar. J. Clean. Prod. 292, 126050 https://doi.org/10.1016/J.JCLEPRO.2021.126050.
Liu, X., Ma, B., Tan, H., Li, H., Mei, J., Zhang, T., Chen, P., Gu, B., 2019. Chloride immobilization of cement-based material containing nano-Al2O3. Constr. Build. Mater. 220, 43–52. https://doi.org/10.1016/J.CONBUILDMAT.2019.05.148.
Liu, Y., Zhu, W., Yang, E.H., 2016. Alkali-activated ground granulated blast-furnace slag incorporating incinerator fly ash as a potential binder. Constr. Build. Mater. 112, 1005–1012. https://doi.org/10.1016/J.CONBUILDMAT.2016.02.153.
Lothenbach, B., Le Saout, G., Gallucci, E., Scrivener, K., 2008. Influence of limestone on the hydration of Portland cements. Cem. Concr. Res. 38, 848–860. https://doi.org/10.1016/j.cemconres.2008.01.002.
Lu, J.X., Poon, C.S., 2018. Use of waste glass in alkali activated cement mortar. Constr. Build. Mater. 160, 399–407. https://doi.org/10.1016/J.CONBUILDMAT.2017.11.080.
Mehta, P.K., Monteiro, P.J.M., 2006. Concrete: Microstructure, Properties, and Materials, Third ed. McGraw-Hill.
Meng, T., Qiang, Y., Hu, A., Xu, C., Lin, L., 2017. Effect of compound nano-CaCO3 addition on strength development and microstructure of cement-stabilized soil in the marine environment. Constr. Build. Mater. 151, 775–781. https://doi.org/10.1016/J.CONBUILDMAT.2017.06.016.
Myers, R.J., L'Hôpital, E., Provis, J.L., Lothenbach, B., 2015. Effect of temperature and aluminium on calcium (alumino)silicate hydrate chemistry under equilibrium conditions. Cem. Concr. Res. 68, 83–93. https://doi.org/10.1016/J.CEMCONRES.2014.10.015.
Nikravan, M., Ramezanianpnour, A.A., Maknoon, R., 2018. Technological and environmental behavior of petrochemical incineration bottom ash (PI-BA) in cement-based using nano-SiO2 and silica fume (SF). Constr. Build. Mater. 191, 1042–1052. https://doi.org/10.1016/J.CONBUILDMAT.2018.09.135.
Pacheco Torgal, F., Miraldo, S., Labrincha, J.A., De Brito, J., 2012. An overview on concrete carbonation in the context of eco-efficient construction: Evaluation, use of SCMs and/or RAC. Constr. Build. Mater. 36, 141–150. https://doi.org/10.1016/J.CONBUILDMAT.2012.04.066.
Provis, J.L., van Deventer, J.S.J., 2019. Geopolymers and other alkali-activated materials, 5th ed, Lea's Chemistry of Cement and Concrete. Elsevier Ltd. 10.1016/b978-0-08-100773-0.00016-2.
Qing, Y., Zenan, Z., Deyu, K., Rongshen, C., 2007. Influence of nano-SiO2 addition on properties of hardened cement paste as compared with silica fume. Constr. Build. Mater. 21, 539–545. https://doi.org/10.1016/J.CONBUILDMAT.2005.09.001.
Quercia, G., Hüsken, G., Brouwers, H.J.H., 2012. Water demand of amorphous nano silica and its impact on the workability of cement paste. Cem. Concr. Res. 42, 344–357. https://doi.org/10.1016/J.CEMCONRES.2011.10.008.
Ramezanianpour, A.A., Moeini, M.A., 2018. Mechanical and durability properties of alkali activated slag coating mortars containing nanosilica and silica fume. Constr. Build. Mater. 163, 611–621. https://doi.org/10.1016/J.CONBUILDMAT.2017.12.062.
Renaudin, G., Russias, J., Leroux, F., Frizon, F., Cau-dit-Coumes, C., 2009. Structural characterization of C-S-H and C-A-S-H samples-Part I: Long-range order investigated by Rietveld analyses. J. Solid State Chem. 182, 3312–3319. https://doi.org/10.1016/j.jssc.2009.09.026.
Richardson, I.G., 2008. The calcium silicate hydrates. Cem. Concr. Res. 38, 137–158. https://doi.org/10.1016/J.CEMCONRES.2007.11.005.
Rupasinghe, M., San Nicolas, R., Mendis, P., Sofi, M., Ngo, T., 2017. Investigation of strength and hydration characteristics in nano-silica incorporated cement paste. Cem. Concr. Compos. 80, 17–30. https://doi.org/10.1016/J.CEMCONCOMP.2017.02.011.
Sevelsted, T.F., Skibsted, J., 2015. Carbonation of C – S – H and C – A – S – H samples studied by 13 C, 27 Al and 29 Si MAS NMR spectroscopy. Cem. Concr. Res. 71, 56–65. https://doi.org/10.1016/j.cemconres.2015.01.019.
Shi, C., Day, R.L., 1995. A calorimetric study of early hydration of alkali-slag cements. Cem. Concr. Res. 25, 1333–1346. https://doi.org/10.1016/0008-8846(95)00126-W.
Shi, C., Krivenko, P. V., Roy, D., 2003. alkali-activated cements and concretes, 1st Editio. ed. London. 10.1201/9781482266900.
Shi, C., Jiménez, A.F., Palomo, A., 2011. New cements for the 21st century: The pursuit of an alternative to Portland cement. Cem. Concr. Res. 41, 750–763. https://doi.org/10.1016/J.CEMCONRES.2011.03.016.
Shi, C., Qian, J., 2000. High performance cementing materials from industrial slags — a review. Resour. Conserv. Recycl. 29, 195–207. https://doi.org/10.1016/S0921-3449(99)00060-9.
Shi, Z., Shi, C., Wan, S., Li, N., Zhang, Z., 2018a. Effect of alkali dosage and silicate modulus on carbonation of alkali-activated slag mortars. Cem. Concr. Res. 113, 55–64. https://doi.org/10.1016/j.cemconres.2018.07.005.
Shi, Z., Shi, C., Wan, S., Zhang, Z., 2018b. Effects of alkali dosage and silicate modulus on alkali-silica reaction in alkali-activated slag mortars. Cem. Concr. Res. 111, 104–115. https://doi.org/10.1016/J.CEMCONRES.2018.06.005.
Shirley, R., Black, L., 2011. Alkali activated solidification/stabilisation of air pollution control residues and co-fired pulverised fuel ash. J. Hazard. Mater. 194, 232–242. https://doi.org/10.1016/J.JHAZMAT.2011.07.100.
Singh, L.P., Zhu, W., Howind, T., Sharma, U., 2017. Quantification and characterization of C-S-H in silica nanoparticles incorporated cementitious system. Cem. Concr. Compos. 79, 106–116. https://doi.org/10.1016/J.CEMCONCOMP.2017.02.004.
Sumajouw, D.M.J., Hardjito, D., Wallah, S.E., Rangan, B.V., 2007. Fly ash-based geopolymer concrete: Study of slender reinforced columns. J. Mater. Sci. 42, 3124–3130. https://doi.org/10.1007/s10853-006-0523-8.
Uddin, F., Shaikh, A., Hosan, A., 2019. Effect of nano silica on compressive strength and microstructures of high volume blast furnace slag and high volume blast furnace slag- fly ash blended pastes. Sustain. Mater. Technol. 17, e00111.
Valente, M., Sambucci, M., Chougan, M., Hamidreza, S., 2022. Reducing the emission of climate-altering substances in cementitious materials : A comparison between alkali-activated materials and Portland cement-based composites incorporating recycled tire rubber. J. Clean. Prod. 333, 130013 https://doi.org/10.1016/j.jclepro.2021.130013.
Walling, S.A., Bernal, S.A., Gardner, L.J., Kinoshita, H., Provis, J., 2018. Blast furnace slag-Mg(OH)2 cements activated by sodium carbonate. RSC Adv. 8, 23101–23118. https://doi.org/10.1039/c8ra03717e.
Wang, S.Y., McCaslin, E., White, C.E., 2020a. Effects of magnesium content and carbonation on the multiscale pore structure of alkali-activated slags. Cem. Concr. Res. 130, 105979 https://doi.org/10.1016/J.CEMCONRES.2020.105979.
Wang, S.-D., Pu, X.-C., Scrivener, K.L., Pratt, P.L., 1995. Alkali-activated slag cement and concrete: a review of properties and problems. Adv. Cem. Res. 7, 93–102. https://doi.org/10.1680/adcr.1995.7.27.93.
Wang, Y., Shao, Y., Darko, M., Whalen, J.K., 2016. Recycling combustion ash for sustainable cement production : A critical review with data-mining and time-series predictive models. Constr. Build. Mater. 123, 673–689. https://doi.org/10.1016/j.conbuildmat.2016.07.031.
Wang, Z., Yu, Q., Gauvin, F., Feng, P., Qianping, R., Brouwers, H.J.H., 2020b. Nanodispersed TiO2 hydrosol modified Portland cement paste: The underlying role of hydration on self-cleaning mechanisms. Cem. Concr. Res. 136, 106156 https://doi.org/10.1016/j.cemconres.2020.106156.
Weil, M., Dombrowski, K., Buchwald, A., 2009. Life-cycle analysis of geopolymers. Geopolym. Struct. Process. Prop. Ind. Appl. 194–210 https://doi.org/10.1533/9781845696382.2.194.
Yang, K.H., Cho, A.R., Song, J.K., Nam, S.H., 2012. Hydration products and strength development of calcium hydroxide-based alkali-activated slag mortars. Constr. Build. Mater. 29, 410–419. https://doi.org/10.1016/j.conbuildmat.2011.10.063.
Yang, T., Zhang, Z., Zhu, H., Zhang, W., Gao, Y., Zhang, X., Wu, Q., 2019. Effects of calcined dolomite addition on reaction kinetics of one-part sodium carbonate-activated slag cements. Constr. Build. Mater. 211, 329–336. https://doi.org/10.1016/j.conbuildmat.2019.03.245.
Ye, H., Chen, Z., Huang, L., 2019. Mechanism of sulfate attack on alkali-activated slag : The role of activator composition. Cem. Concr. Res. 125, 105868 https://doi.org/10.1016/j.cemconres.2019.105868.
Yu, P., Kirkpatrick, R.J., Poe, B., McMillan, P.F., Cong, X., 1999. Structure of Calcium Silicate Hydrate (C-S-H): Near-, Mid-, and Far-Infrared Spectroscopy. J. Am. Ceram. Soc. 82, 742–748. https://doi.org/10.1111/j.1151-2916.1999.tb01826.x.
Yuan, B., Straub, C., Segers, S., Yu, Q.L., Brouwers, H.J.H., 2017a. Sodium carbonate activated slag as cement replacement in autoclaved aerated concrete. Ceram. Int. 43, 6039–6047. https://doi.org/10.1016/j.ceramint.2017.01.144.
Yuan, B., Yu, Q.L., Brouwers, H.J.H., 2017b. Time-dependent characterization of Na2CO3 activated slag. Cem. Concr. Compos. 84, 188–197. https://doi.org/10.1016/j.cemconcomp.2017.09.005.
Yuan, Q., Zhou, D., Li, B., Huang, H., Shi, C., 2018. Effect of mineral admixtures on the structural build-up of cement paste. Constr. Build. Mater. 160, 117–126. https://doi.org/10.1016/J.CONBUILDMAT.2017.11.050.
Zhao, Y., Shi, T., Cao, L., Kan, L., Wu, M., 2021. Influence of steel slag on the properties of alkali-activated fly ash and blast-furnace slag based fiber reinforced composites. Cem. Concr. Compos. 116, 103875 https://doi.org/10.1016/J.CEMCONCOMP.2020.103875.
Živica, V., 2007. Effects of type and dosage of alkaline activator and temperature on the properties of alkali-activated slag mixtures. Constr. Build. Mater. 21, 1463–1469. https://doi.org/10.1016/J.CONBUILDMAT.2006.07.002.